Check for updates

ADVANCED INTELLIGENT SYSTEMS
Open Access
www.advintellsyst.com

Multistable Soft Robots Assembled from Bistable Auxetic Building Blocks

*Bojian Zhang, Zhiqiang Meng, Xudong Yang, Yiran Zhang, Tianyu Chen, Yu Chen, and Yifan Wang**

Soft robotics have significantly influenced both scientific and industrial domains over the past decades. However, their inherent limitations of material or structural softness pose a persistent challenge in terms of shape retention and load capacity for various applications. To address this challenge, bistable and multistable structures with two or more mechanically stable states and snap-through switchability emerge as a promising solution. Herein, a multistable soft robot design assembled from bistable auxetic building blocks with negative Poisson's ratio and a large volumetric change is presented. The bistable mechanical behavior and optimal structural parameters have been investigated by mechanical modeling, finite element analysis, and experimental testing. To demonstrate the shape retention ability and enhanced load capacity of our robotic design, a multistable manipulator with a low-complexity closed-loop control system is presented, capable of maintaining 216 discrete stable states even when the pneumatic pressure supply is removed. To validate the multifunctionality of design, a multistable tube crawler with a notable load capacity of approximately five times its own body weight is developed.

1. Introduction

In contrast to conventional robots, soft robots distinguish themselves with their excellent abilities to morph shapes under substantial deformations, vary stiffnesses, and seamlessly adapt to human-centric environments.[1–8] To date, most soft robotic systems utilize soft materials or structures to guide continuum deformation and achieve desired configurations.[9–14] As a result, a significant challenge for continuum soft robotics lies in their dependence on a continuous power supply to maintain their intended forms or rigidity. If the power supply is interrupted (i.e., the sealing membrane is punctured in pneumatic or hydraulic systems), these robots tend to revert to their initial shapes and stiffnesses due to elasticity, which in some instances may incur structural damage or even safety hazards.[15,16] To address this issue, robots with multistable configurations that can maintain discrete stable states without external energy inputs are highly desired, as their shape-locking ability offers a promising solution to the limitations of continuum-deformation soft robots.[17–19]

To achieve shape-locking capabilities in soft robots, researchers have explored various materials and actuation methods, with bistable structures emerging as a prevalent approach. Previous works have utilized bistable structures to achieve various robotic applications, including 1D buckled beam-based soft bistable and multistable actuators,[20–24] 2D curved plate-based soft bistable actuators for gripper applications,[25–27] and 3D dome-type shell-based structures as jumping actuators.[28–30] However, these existing bistable actuators only function as single units with limited locomotion versatility, unable to achieve intricate movement patterns. To improve their functionality, a promising solution lies in modular design, which offers a pathway toward controllable multistable soft robots.[18,19,22,27,31] By engineering the assembly of individual bistable auxetic building blocks, the modular approach could enable the realization of complex locomotion patterns and diverse robot configurations with good shape retention ability and enhanced load capacity.[22,32–34]

In this study, we introduce a soft robot design assembled from bistable auxetic building blocks with negative Poisson's ratio and large volumetric change (≈8 times) between the folded and deployed states (**Figure 1**b). We investigated the snap-through behavior and mechanical stability through theoretical modeling, finite element analysis (FEA), and experiments. For robotic applications, we designed a multistable manipulator with inherent shape lockability in the event of a power supply shutdown (Figure 1c). To enhance its functionality, we implemented a closed-loop control system grounded in computer vision, incorporating jog input and hand-tracking input. Additionally, we developed a lightweight tube crawler utilizing the bistable element as its anchor point to demonstrate the versatility of our design (Figure 1d). The load capacity can be customized by adjusting the anchor numbers accordingly. This study presents a feasible paradigm to design multistable soft robots

B. Zhang, Z. Meng, X. Yang, Y. Zhang, T. Chen, Y. Chen, Y. Wang
School of Mechanical and Aerospace Engineering
Nanyang Technological University
Singapore 639798, Singapore
E-mail: yifan.wang@ntu.edu.sg

The ORCID identification number(s) for the author(s) of this article can be found under https://doi.org/10.1002/aisy.202400529.

© 2024 The Author(s). Advanced Intelligent Systems published by Wiley-VCH GmbH. This is an open access article under the terms of the Creative Commons Attribution License, which permits use, distribution and reproduction in any medium, provided the original work is properly cited.

DOI: 10.1002/aisy.202400529

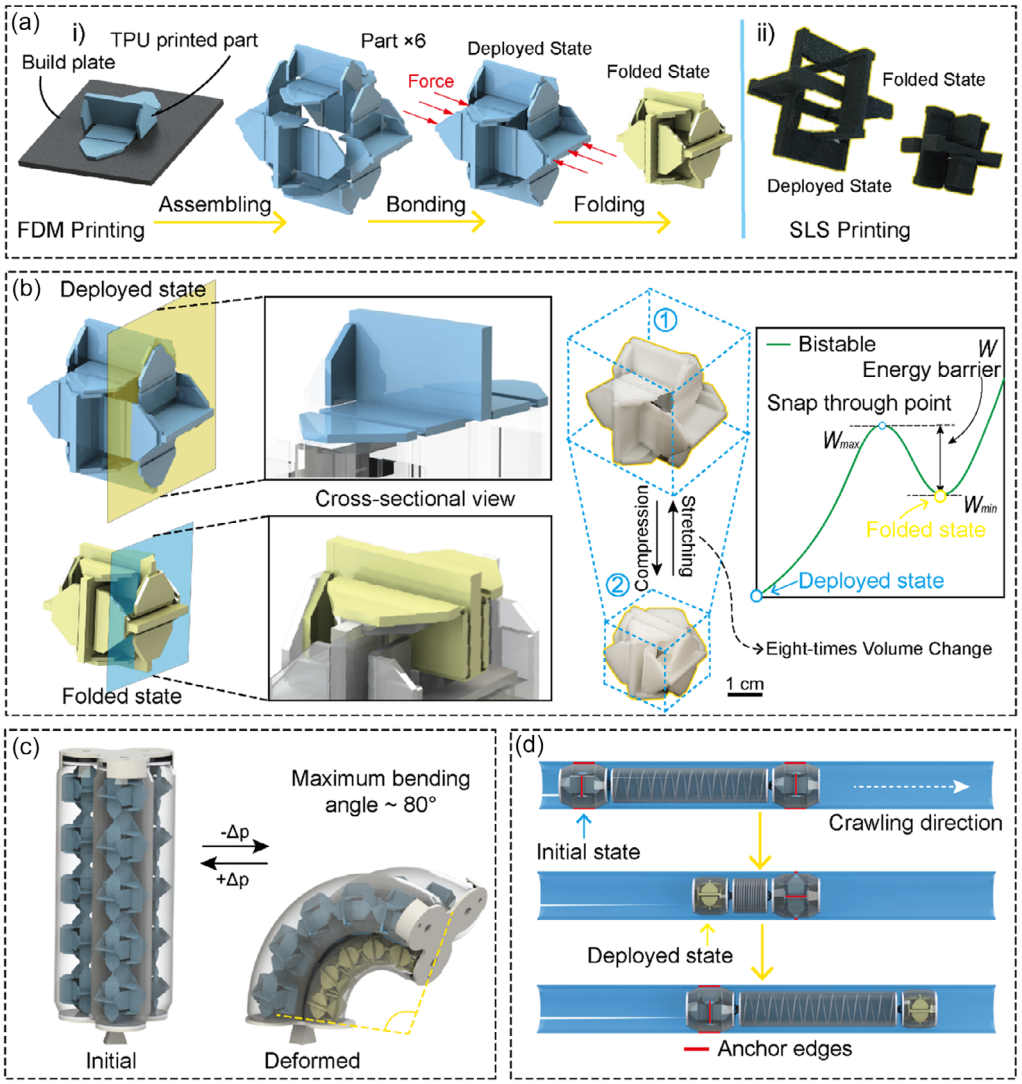


Figure 1. Bistable auxetic building block design and fabrication. a) Two fabrication methods for the block: (i) FDM fabrication involves three steps: 3D printing each part using TPU filament, manually assembling the six parts, and bonding them together with glue; (ii) SLS fabrication: blocks are printed in one step using TPU powder. b) Illustration depicting the bistable auxetic building block in its deployed and folded states, exhibiting an eight-times volume change experimentally. Additionally, the energy landscape of the block is shown. c) Multistable manipulator with maximum bending angle ≈80° in initial and deployed configuration. d) Illustration on steps of bistable crawler locomotion: the back anchor and elongation part shrinking; the back anchor deploying and front anchor shrinking with elongation part extending; the front anchor deploying with whole crawler restore.

capable of maintaining their shapes with high load capacity without the need for continuous power input.

2. Results

2.1. Design, Fabrication, and Mechanism of the Bistable Auxetic Building Block

Bistable structures have been extensively investigated in previous studies. However, most of these bistable structures are based on one- or two-dimensional elements, such as buckled beams and curved shells. While some three-dimensional structures such as bistable dome shells have been explored,[35–40] they still only have one-dimensional locomotion. These problems make them unsuitable to serve as building blocks for robots that can deform and function in all dimensions. To address this issue, we here introduce a three-dimensional (3D) bistable building block exhibiting auxetic characteristics in all three directions. With the 3D bistable structure, complex robotic locomotion tasks can be achieved, such as the anchor of a tube crawler demonstrated later in this article: with 3D bistable auxetic building blocks as anchors, the robot can achieve both anchoring abilities in the radial direction and locomotion ability in longitudinal direction.

We used two fabrication methods for the bistable auxetic building blocks. The first method involved using a fused deposition modeling (FDM) 3D printer with thermoplastic polyurethane (TPU) filament to create the blocks (Figure 1a(i)). Due

© 2024 The Author(s). Advanced Intelligent Systems published by Wiley-VCH GmbH

to their isotropic properties, these structures exhibited symmetry across all six directions. We initially divided the cubic structure into six identical pieces. The 3D block was then assembled by bonding these six pieces together to form the faces of the cube. The second method utilized a selective laser sintering (SLS) 3D printer with TPU powder, allowing us to fabricate the entire block in one step (Figure 1a(ii)). However, due to the better durability of the FDM-printed samples, we use the FDM-printed blocks for our later studies. The cross-sectional view from Figure 1b shows the inner shape of the beam in deployed state and folded state. When in deployed state, the block has the lowest strain energy. Then, when applying a uniaxial compression force in any of the orthogonal face directions, beams in the faces start to buckle, and the strain energy increases. When compressed beyond the snap-through point, the strain energy of the block starts to decrease rapidly till the second minimum energy point (Figure 1b). The bistable mechanism is further explained in the following discussions.

To investigate the underlying mechanisms of the bistable auxetic building block and consider the deformation symmetry of the block, we divided the block into six identical parts and selected one part to establish a theoretical model (**Figure 2**a). We simplified it as a mechanical model consisting of five components: two hinges acting as springs and three beams acting as rigid bars (Figure 2a(iii)). The motion trajectory of the block can be categorized into the deployed state, intermediate state (Figure 2a(iv)), and folded state (Figure 2a(v)). The further details of deformation are presented in Figure S7. The hinge effect can be considered a combination of a torsion spring K_t, which stores energy from bending, and a compression spring K_l, which stores energy from compression, as detailed in Supporting Information S2.1. Additionally, due to the isotropic of block deformation, bars AB and EF have the same displacement u. We established three assumptions to simplify the mechanical model: 1. Hinge BC and DE have the same deformation, donated as $\Delta_{BC} = \Delta_{DE} = \Delta/2$ and bending angel θ; 2. Hinge BC and DE are always collineations with bar CD; 3. For torsion spring, rotation angle θ is equal to $\pi - \theta_{ABC}$; hence, potential energy of hinges according to Hooke's law as

$$W = W_t + W_l = \frac{1}{4}K_l\Delta^2 + K_t\theta^2 \tag{1}$$

where, K_t and K_l represent the coefficient values of the torsion spring and compression spring, respectively. We determined K_t and K_l using a semianalytical method, as detailed in Supporting Information S2.2. After calculations, we can express the dimensionless energy W^* in terms of the dimensionless parameters u/L, t/l and l/L as

$$\begin{aligned} W^* = {} & \lambda_1\left(\frac{t}{l}\right)^2\left(\arctan\frac{\frac{u}{L}}{1+2\frac{l}{L}-\frac{u}{L}}\right)^2 \\ & + \frac{1}{4}\lambda_2\left(\frac{L}{l}\right)^2\left(2\frac{l}{L}+1-\sqrt{\left(1+2\frac{l}{L}-\frac{u}{L}\right)^2+\left(\frac{u}{L}\right)^2}\right) \end{aligned} \tag{2}$$

where λ_1 and λ_2 are fitting parameters for the torsion and compression springs, respectively. We have now established a design guideline for the bistable auxetic building block based on dimensionless parameters u/L, t/l, and l/L. We found that W^* comprises two components: namely, dimensionless energy from the torsion spring and dimensionless energy from the compression spring. For the torsion spring energy, it increases continuously with the bending angle θ. At the same time, the torsion spring consistently stores energy. Based on these observations, we derived the following conclusions: 1. An increase in t/l leads to a significant rise in the energy stored in the torsion spring, causing the bistable block to transition into a monostable state. 2. An increase in l/L results in a considerable expansion of the hinge percentage, reducing the snap-through ability of the bistable block and leading it to gradually transition into a monostable state.

Based on the equation $W^* = W^*(u/l \mid t/l,\ l/L)$ (see Supporting Information S2.2 for details), for bistable case, the potential energy exhibits a nonmonotonic behavior, characterized by an initial increase followed by a decrease and subsequent increase, indicative of the presence of two energy minima. Conversely, as for the monostable case, the potential energy demonstrates a monotonic increase. We can define

$$\eta = \frac{W_{max} - W_{min}}{W_{max}} \tag{3}$$

For bistable cases, $\eta > 0$, whereas for monostable cases, $\eta = 0$. Combining Equation (2) and (3), the contour plots of η in the t/l and l/L are shown in Figure 2b. The solid blue line in Figure 2b is the boundary separating the monostable and bistable regimes of the block. The lower left region (dark blue) represents bistable, and the upper right (yellow) represents monostable. To validate the correctness of our theoretical mechanism, we selected random values of t/l and l/L that correspond to both monostable blocks (blue patterns) and bistable blocks (red patterns). We conducted FEA (marked as squares) and experiments (marked as stars) for these values, and the results showed a good match, confirming the validity of our theory. The measurements on two different auxetic blocks: a bistable block with $l = 1$ mm, $t = 0.2$ mm, and $L = 5$ mm, and a monostable block with $l = 2.5$ mm, $t = 0.3$ mm, and $L = 5$ mm. The results indicate that for the bistable block (Figure 2c), the force–displacement curve first rises and then falls. In contrast, for the monostable block, the force–displacement curve shows a continuous increasing trend. The predictions from FEA align well with the experimental results for these two different stable states.

To illustrate the design versatility of the auxetic block in a programmed transformation structure, we performed experimental measurements on five different auxetic blocks (Figure 2d), each with $t = 0.2$ mm and $L = 5$ mm but varying in l. The results reveal that the peak forces required for switching can be adjusted, and the bistability of the blocks can be confirmed by distinct force regions on the force–displacement curves. When these five bistable auxetic building blocks are connected in series and stretched, the resulting structure sequentially transforms into five preprogrammed shapes. The corresponding stretching force (Figure 2f) exhibits five increasing peaks followed by decreases associated with the snap-through behavior of the blocks.

To control the multistable structure, we encapsulated it within a soft membrane chamber equipped with rigid caps (Figure 2f). Applying negative pressure to the membrane chamber causes

© 2024 The Author(s). Advanced Intelligent Systems published by Wiley-VCH GmbH

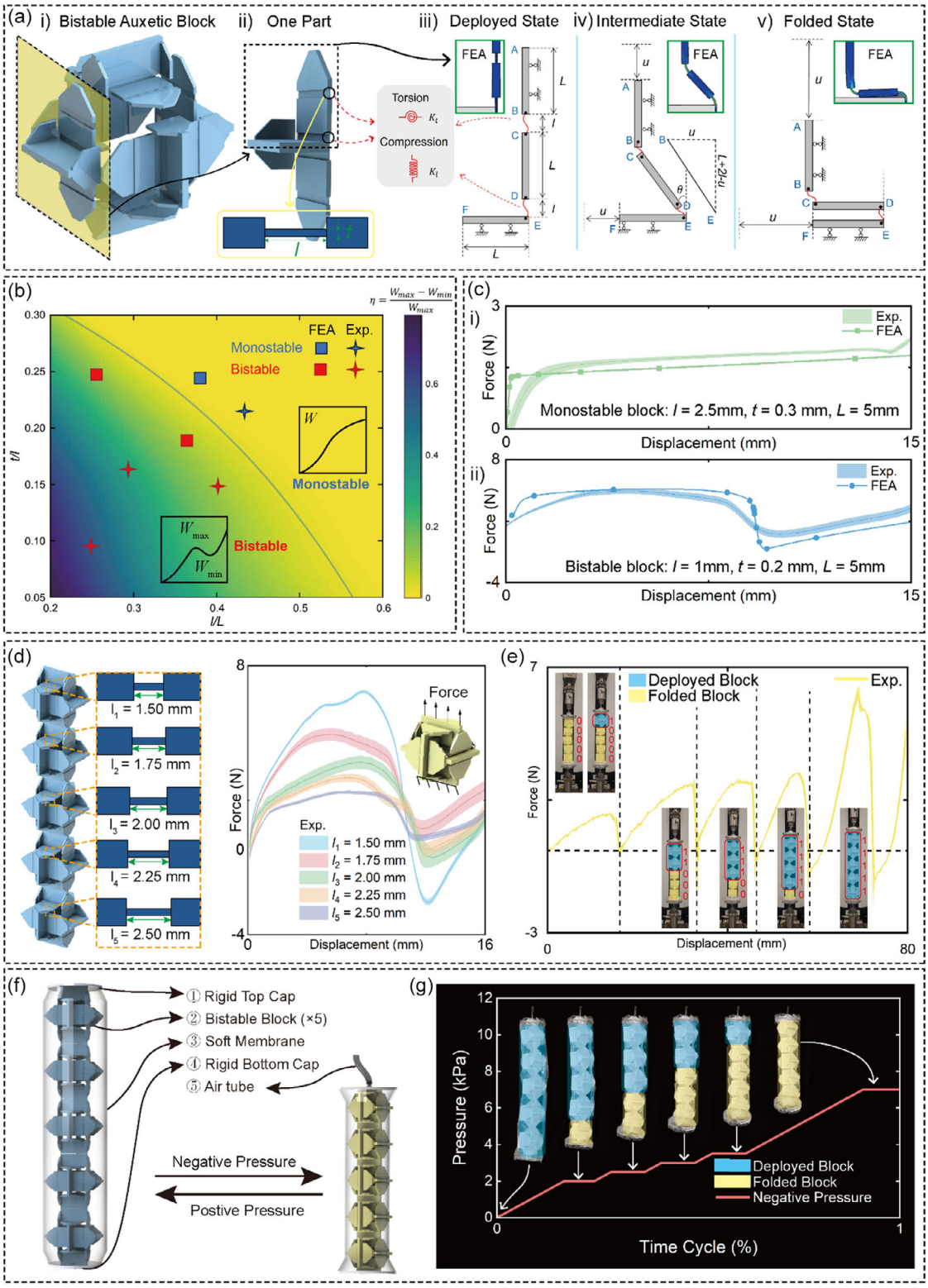


Figure 2. Design and mechanical responses of bistable auxetic building blocks. a) Configuration of the theoretical model and boundary conditions during three typical states. b) Phase diagram and contour map for the factor η in the t/l and l/L. The dark blue to greed region ($\eta > 0$) represents bistable blocks, and the yellow region ($\eta = 0$) represents monostable blocks. c) Force–displacement responses of monostable and bistable cases in FEA and experiment. d) Stretching force as a function of displacement for five bistable auxetic building blocks of different sizes and FEA results are presented in Figure S4. e) Transformation snapshots of a model consisting of five blocks in series and the corresponding relationship between force and displacement. f) Design schematic of a single pneumatic muscle. g) Experimental pressure control curve for the pneumatic muscle.

© 2024 The Author(s). Advanced Intelligent Systems published by Wiley-VCH GmbH

the multistable structure to transition from the deployed state to the folded state. Conversely, when positive pressure is applied to the folded structure, it transitions back to the deployed state. Figure 2g illustrates the relationship between the deformation of the tandem structure and the applied negative pressure. As the negative pressure increases, the blocks fold sequentially, with all five blocks folding by −7 kPa (further details are provided in Figure S9a and Video S8).

2.2. Design and Performance of a Multistable Robotic Manipulator

In most existing soft pneumatic manipulators, when pressure supply stops or membrane puncture happens, they cannot maintain the current shape and, even more critically, structural failure may happen.[16] To address this issue, we demonstrate a 3-degree-of-freedom (3-DOF) multistable manipulator assembled from the bistable auxetic building blocks. The manipulator is constructed by three parallel pneumatic artificial muscles, each of which consists of five bistable auxetic building blocks in linear arrangement (**Figure 3**a). Three bistable arrays are placed 120° apart around the central axis of the manipulator and fixed to two rigid end caps (#3 and #6 in Figure 3a). Each bistable array is covered with a soft membrane (#5, Figure 3a) to form an air-tight pneumatic muscle. Three pneumatic muscles are connected to rigid top and bottom connectors. The rigid bottom plate is mounted on the base of a commercial robotic arm (see Experimental Section for details). In addition, three optical markers are connected to the top plate for motion capture. We can control the contraction and expansion of the artificial muscles by applying negative and positive pressures as the soft membranes provide an airtight internal volume. The diameter of each artificial muscle is 50 mm, while the centers of three pneumatic muscles are located on a 60 mm-diameter circle.

Figure 3b demonstrates four general postures: vertical initial posture (Figure 3b(i)), bending postures of $\varphi = 60°$, $\beta = 64°$ (Figure 3b(ii)), $\varphi = 0°$, $\beta = 64°$ (Figure 3b (iii)), and $\varphi = -60°$, $\beta = 64°$ (Figure 3b(iv)). The manipulator length is 200 mm in straight configuration without connector structures. At the initial state, the pneumatic muscle shrinks to a minimum length of 140 mm at −80 kPa. When the pneumatic muscle is mounted into the manipulator body, the contraction of one muscle results in the bending motion of the robotic manipulator toward the contracted pneumatic muscle. However, continuously changing the pressure will not cause a continuously bending reaction of the manipulator since the bistable pneumatic muscle can only shrink to discrete lengths. When two pneumatic muscles are actuated simultaneously, the manipulator bends toward the direction between the two actuated muscles. By regulating the pressure of all three pneumatic muscles, respectively, the manipulator achieves a 2-DOF motion (i.e., bending and swing) (Figure 3b). In addition, when three pneumatic muscles shrink together, the manipulator length has an expansion and contraction degree of freedom. Hence, the manipulator can achieve a total of 3-DOF.

The manipulator's bending angle is directly controlled by the number of bistable blocks in the folded or deployed states. With the increasing number of units being folded, the bending angle linearly increases by 16° every step from 0° to 80° (Figure 3c). And relationship between bending curvature and applied pressure is presented in Figure S9b. Since the volume and length change of each bistable auxetic building block is constant, the bending angle change is also constant during each step. Hence, the bistable mechanism provides a high robustness for controlling the system. By controlling the discrete stable states of the multistable manipulator, we can operate the manipulator along distinct circular paths (Figure 3d). The diameters of different circular paths increase with the number of units being folded in the actuated muscle, where the green circle presents the maximum bending angle with all five bistable units folded. In contrast, the blue circle presents the minimum bending angle with only one bistable unit folded.

The load capacity of the manipulator is further demonstrated in Figure 3e,f. With negative pressure of −80 kPa, the manipulator can lift 4 kg maximum weight with 50 mm length of contraction, compared to 60 mm contraction with free load (Figure 3e and Video S1). More importantly, due to the multistable characteristics of the artificial muscles, they can retain position under load even when the negative pressure supply is removed. Figure 3f illustrates the shape retention ability of the multistable manipulator. When lifting a 200 g weight with −80 kPa, the manipulator will contract by 62 mm (see Video S1 for details). Then we removed the negative pressure supply and observed that the bistable units did not experience snap-though transition and remained in the folded state. This behavior offers a potential solution to reducing energy consumption and preventing sudden collapses caused by bursts or punctures in soft pneumatic robots. To assess the shape retention ability of the multistable manipulator, we positioned it at its maximum bending angle and exposed it to atmospheric conditions to simulate an air leakage scenario. We captured images of the manipulator at half-day intervals, as shown in Figure 3g. The minimal deformation observed indicates that the manipulator possesses excellent shape retention capability.

2.3. Low-Complexity Closed-Loop Control System for the Multistable Manipulator

Compared to existing soft robotic structures with continuous deformations, our developed multistable robotic structures offer multiple mechanically stable configurations which yield several benefits, including reducing control complexity and enhancing energy efficiency. Unlike continuum manipulators that require continuous control and power input to reach target positions, our multistable manipulators are engineered to naturally maintain stable and discrete positions. Once a stable position is reached, the energy input can be stopped to facilitate power conservation. In this context, we successfully implement a low-complexity closed-loop control system with motion capture cameras that can effectively and precisely control the manipulator's movements.

The key elements of the control system for the multistable manipulator are illustrated in **Figure 4**a. For motion detection, we utilized a motion capture system (OptiTrack Inc) to track the position of three markers mounted on the manipulator's end. The position information was processed and generated

© 2024 The Author(s). Advanced Intelligent Systems published by Wiley-VCH GmbH

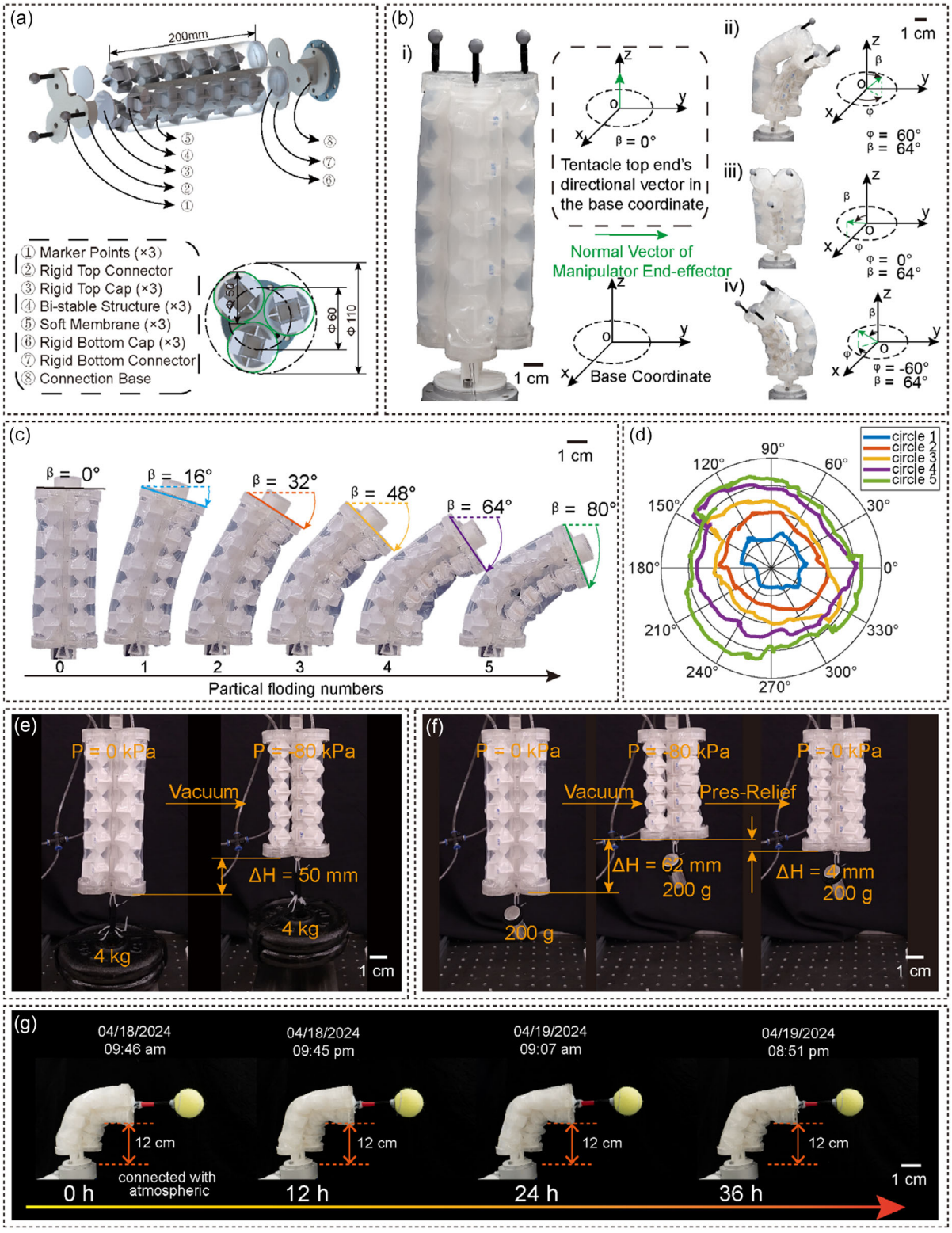


Figure 3. Design and movements of a multistable robotic manipulator. a) Exploded view and cross-sectional diagram of the multistable manipulator. b) Coordinates and a few postures representing the bending and swinging motion of the multistable manipulator actuated by a pneumatic control system. c) Relationship between folded block numbers and bending angle. d) Path tracking results of different folded block numbers. e) Maximum manipulator carrying capacity. f) Loading capacity and contraction distance of the multistable manipulator in two stable states, which maintains contraction even when negative pressure is relieved. g) Manipulator long-term shape retention ability (connected with atmospheric) experiment.

© 2024 The Author(s). Advanced Intelligent Systems published by Wiley-VCH GmbH

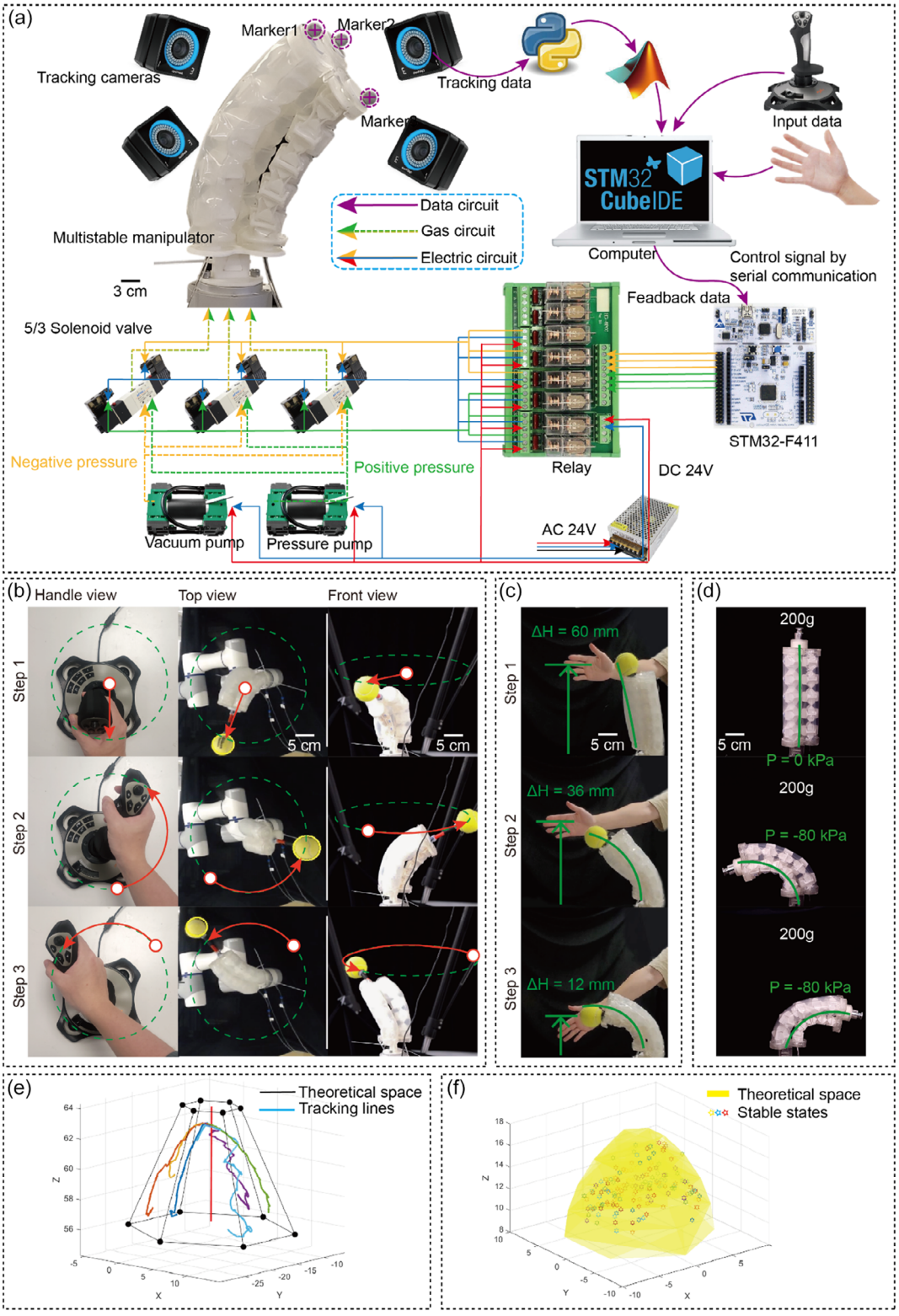


Figure 4. Low-complexity closed-loop control system for the multistable manipulator. a) Experimental setup for the closed-loop control of the multistable manipulator (dish lines in yellow and green lines represent the negative and positive gas flows for the three multistable pneumatic muscles, respectively, solid lines in yellow and green represent the electric flows for the three 5/3 solenoid valves, and purple flow lines represent the tracking data flows). b) Snapshots of the handle-controlled manipulation. c) Snapshots of the human hand path tracking. d) Bending angle of multistable manipulator when maximum 200 g payload applied. e) Theoretical working space and experimental tracking paths. f) The experimental stable states in the manipulator working space.

© 2024 The Author(s). Advanced Intelligent Systems published by Wiley-VCH GmbH

as reference data. Two control signal inputs were established by a handle and a control algorithm. These signals were transmitted to a microcontroller unit via serial communication. The microcontroller unit converted these signals into electrical frequencies to control relays, which, in turn, managed three 5/3 solenoid valves. These valves regulated the supply of negative and positive pressures from air pumps to the three pneumatic muscles. Additionally, an DC power source provided 24 V DC electronic power to the relays and pumps. The specifics of the control algorithm design and detailed methodologies are detailed in Figure S5.

Due to its multistable nature, the robotic manipulator does not need continuous energy consumption or actuation inputs to maintain the stable states. In our experiment, we took this advantage to design a low-complexity close-loop control system for the multistable manipulator. There are $6^3 = 216$ stable states of the multistable manipulator, since the three pneumatic muscles each has six discrete stable lengths. The control method involves comparing captured data with initial coordinates to set a target within a 1 mm error range. It also uses a pixel error range for the motion capture system. The system takes two input signals: one for the manipulator's current position and another for the handle's position. Algorithm then calculates the distance and direction to the target and identifies the most efficient path to reach it.

In essence, the control method involves comparing captured data with theoretical coordinates, assessing deviations, and using an algorithm to calculate the direction and distance needed to guide the manipulator toward the desired target position. This approach ensures precise and efficient control of the manipulator's movements. For example, if the current position is located in the center of the polar coordinate, and the target position is located in $\theta = 60°$, $r = 45$ mm, the control system sends signals to relay the leading valve which controls the pneumatic muscle located in 60° direction vacuuming toward to target direction. For another example, which current position is located in $\theta = 60°$, $r = 45$ mm, and the target position is $\theta = 240°$, $r = 45$ mm, the control system sent signals to relay to apply negative pressures to the pneumatic muscles which are located in 180° and 300°, and apply positive pressure to the pneumatic muscle located in 60°. Once the camera detects the marker located within the five-pixel circle around the target position, the system sends signals to the relay to switch off the pneumatic circuit. If the camera observes the marker exceeds the target position, the system will send signals to switch on the pressure circuit for the pneumatic muscles located in 180° and 300° to make them reduce bending angle.

The experimental setup and outcomes of the control system operations are shown in Figure 4b and Video S2. The first column depicts the handle's directional movements. A green arrow in the top view (in polar coordinates) represents the handle's bending direction. In the first row, pulling the handle to 180° supplied negative pressure to the pneumatic muscle at that location. This causes the manipulator to bend accordingly. The accompanying experimental images in the top and front views illustrate this process. Similar actions are performed in the second and third rows, bending the manipulator to 60° and 300°, respectively, by manipulating the handle.

Figure 4c illustrates an experiment involving a hand-tracking control system. The underlying principle of hand tracking parallels that of handle control. Initially, distinct locations of the hand within the capture space are marked. The algorithm then calculates the distance between the target and current hand positions, providing corresponding signals accordingly. When the difference between the target and current positions is positive, additional negative pressure is applied to specific pneumatic muscles. Conversely, if the difference is negative, the negative pressure ceases, and positive pressure is introduced to correct the curvature. Three-hand altitudes—12, 36, and 60 mm—are chosen for tracking. The manipulator swiftly follows the hand's movements with high precision, as showcased in Video S3.

The multistable manipulator exhibits a maximum operating payload capacity of 200 g without experiencing structural failure or significant deformation beyond its operational limits, supported by −80 kPa pressure on the pneumatic muscles (Figure 4d). To evaluate its controllable maximum bending manipulation performance, we conducted a bending test with a 60° maximum bending angle and tracked the manipulator's motion within the Cartesian coordinate system. We compared the results with the theoretically calculated working space, represented by the black hexagonal platform (Figure 4e). Due to the interaction between the three pneumatic muscles, there are slight deviations between the theoretical and actual working spaces. In addition, we identified the manipulator's 216 stable states and depicted them in Figure 4f as individual-colored points. This figure demonstrates that all these stable states are evenly distributed and well-covered within the theoretical working space, showcasing all the achievable configurations of the multistable manipulator.

Table 1. Comparison of the performance between the multistable robotic manipulator and other soft robotic manipulators.

Name	Loading capacity	Stable states	Maximum bending angle	Shape retention	Close-loop control
[41]	2.8 N a glass of water (≈445 g)	/	≈135°	No	No
[42]	24.6 N (one chamber), 47.1 N (three chambers)	/	120° (one chamber), 80° (two chambers)	No	No
[43]	528 g	/	99.6° (X-axis), 46.2° (Y-axis)	No	No
[44]	200 g	/	90°	No	No
[45]	50 g	/	≈88° (3 V), ≈57° (2 V), ≈26° (1.5 V), ≈16° (1 V)	No	No
[19]	/	8	21.7° ± 0.3° (one unit), 107.8° (four units), 360° (twelve units)	Yes	No
[18]	/	/	≈80°	Yes	No
[17]	/	/	27.3° (each unit)	No	No
[46]	3 kg	/	≈70°	No	Yes
[16]	/	32	≈71°	Yes	No
This work	4 kg	216	80°	Yes	Yes

© 2024 The Author(s). Advanced Intelligent Systems published by Wiley-VCH GmbH

Our multistable robotic manipulator is assembled using bistable auxetic building blocks that possess bistability and volumetric-changing capabilities. Therefore, we compared our performance across several aspects, including number of stable states (for multistable structures), loading capacity, bending angle, shape retention, and closed-loop control capability. In this study, we demonstrated significant advantages in the number of multistable states, loading capacity, and shape retention ability. Additionally, we achieved closed-loop control using a motion capture system, enabling the manipulator to execute rapid movements within seconds. **Table 1** outlines the performance differences between our work and other soft manipulators.

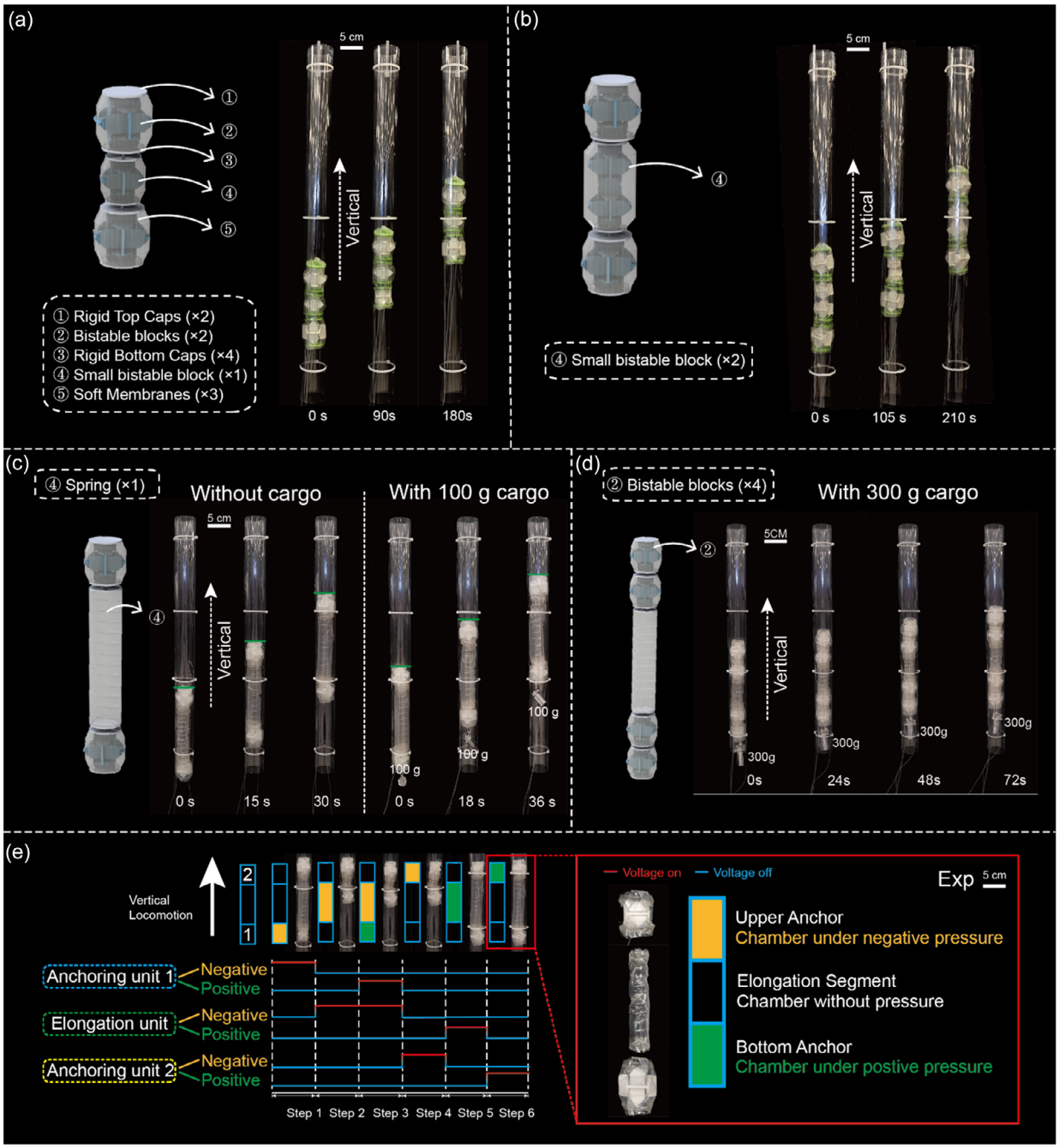


Figure 5. Design and controlled locomotion of a bistable tube crawler. a) Schematic of the bistable tube crawler with single bistable block as elongation segment and snapshots of the crawler locomotion. b) Schematic of the bistable tube crawler with double bistable blocks as elongation segments and snapshots of the crawler locomotion. c) Schematic of the bistable tube crawler with spring as elongation segment and snapshots of the crawler locomotion. d) Schematic of the spring elongation bistable tube crawler with four bistable block anchors and spring as elongation segment and snapshots of the crawler locomotion with 300 g cargo (design details are presented in Figure S6). e) Steps of crawling and sequence of positive and negative pressures used in each pneumatic control channel.

© 2024 The Author(s). Advanced Intelligent Systems published by Wiley-VCH GmbH

2.4. Tube-Crawling Robot with High Load Capacity

Traditional tube crawlers require a substantial force to achieve efficient anchoring during climbing. Utilizing our bistable units as anchors for a tube-crawling robot has several advantages, including enhanced energy efficiency, mechanical stability, and a fail-safe protection mechanism. In this context, we demonstrate a tube-crawling robot that leverages the bistable auxetic building blocks as anchoring points to deliver a vertical load capacity as high as 5 times its self-weight (**Figure 5**d).

Figure 5a illustrates the principal components of the tube-crawling robot, which comprises two bistable anchors connected by a flexible elongation segment. This segment is formed by a bistable auxetic building block, whose volume is reduced to 0.8 times its original size when enclosed in a soft membrane. The bistable units serve as the primary structural elements of the anchor, enabling the crawler to lock into position without the need for a continuous energy supply. This characteristic not only reduces overall energy consumption but also extends the lifespan of the power source. Furthermore, the bistable anchors exhibit quick snap-though behavior, offering rapid responses that are beneficial in scenarios where the crawler must promptly adapt to changing environments. We tested the speed of a single bistable block crawler, which was $\approx$0.006 BL s^{-1} (as shown in Video S4). However, when we increased the number of bistable blocks to two in the elongation segment, the speed decreased to 0.005 BL s^{-1} (as shown in Video S4). This phenomenon occurs because increasing the number of bistable blocks does not affect the strain of the elongation segment due to the fixed extension rate of bistable auxetic building blocks. Consequently, during one cycle, a longer elongation segment requires more time for the vacuum process.

To increase the crawling speed of the tube crawler, we designed an elongation segment with a significantly higher extension rate. This new segment combines a spring as the main structure in the mid-segment, as illustrated in Figure 5c. The experiment in the right side of Figure 5c describes the crawler's vertical locomotion. In an unloaded state, it achieves a top speed of $\approx$0.1 BL s^{-1} (Video S5). When a 100 g weight is applied to the crawler, the speed decreases slightly to 0.09 BL s^{-1} (Video S6). For applications requiring higher load capacity, additional bistable anchors can be added to both the top and bottom of the crawler to increase anchoring force. Figure 5d and Video S6 depict the increased load capacity of 300 g with the inclusion of double bistable anchors. This load capacity surpasses the crawler's self-weight by more than five times, with only 10 g self-weight increase compared to the single anchor type. To verify the crawler's adaptability in different work environments, we conducted an experiment using a soft tube made of low-density ployethylene, as shown in Video S7. During the crawling process in the soft tube, the crawler maintained a consistent speed of $\approx$0.005 BL s^{-1}. This result demonstrates the crawler's ability to operate effectively in varied and flexible environments, maintaining reliable performance across different conditions.

The control loop illustrated in Figure 5e outlines a series of coordinated actions of the tube-crawling robot. Initially, anchoring unit 1, positioned at the bottom, without vacuuming, firmly adheres it to the surface. After the first step, the negative valve is closed, while the bistable cube remains in a folded state. Subsequently, negative pressure is applied to the elongation unit, resulting in its contraction and the upward motion of unit 1. This negative pressure persists until step 3, where anchoring unit 1 is subjected to positive pressure, deploying the bistable structure, and firmly anchoring it to the tube. Following this deployment, anchoring unit 1 contracts, and anchoring unit 2 folded with negative pressure. Then the elongation unit extends, and anchoring unit 2 is subjected to positive pressure to achieve deployed state. After step 6, one cycle completes.

In the cases of power interruptions or system malfunctions, the crawler maintains a stable position, preventing it from detaching or falling from the tube. The bistable cube plays a pivotal role in serving as a fail-safe mechanism, ensuring the crawler's stability and reliability under adverse conditions. This control loop provides a robust and adaptable solution for the crawler's operation, offering a degree of autonomy and safety even in challenging scenarios.

3. Conclusion

In this work, we introduce a multistable manipulator with bistable auxetic building blocks to achieve shape retention ability and enhanced load capacity. The functions are enabled by shape-locking ability of the auxetic bistable blocks and a low-complexity closed-loop control system. Through the motion tracking data of the manipulator, we find that 216 stable states and closed-loop control can be achieved. In addition, with mechanical tests, we verified that the multistable manipulator has good shape-locking ability compared to existing soft pneumatic manipulator. This indicates that the multistable robot is feasible for energy-efficient applications and avoiding failure upon pneumatic enclosing puncture. Furthermore, we also exemplified our design's versatility by developing a multistable tube crawler with as high as 5 times its own weight load capacity.

The concept introduced here addresses existing challenges in soft robotics. Current soft bodies have limitations in shape retention and load capacity, which may cause low energy efficiency and puncture collapse. In addition, the design enables multifunctional and versatile soft robotic applications. The advantages of bistable auxetic building blocks in multistable soft robots are capitalized on two aspects: achieving shape-locking ability and multifunctional design.

While the current bistable cube exhibits unique characteristics and versatility, it comes with some challenges. The multistable manipulator, for instance, can achieve position maintenance and control locomotion but remains to be a manipulator with discrete movement steps. This means it cannot attain the same level of motion smoothness and continuous motion as a continuum manipulator. We believe this problem can be solved by increasing the density of block to approximate a continuum control system. Additionally, the fabrication method, based on FDM, imposes limitations. With this approach, we are unable to print the entire cube in one piece. Instead, we must divide the cube into six identical pieces for separate printing and subsequent manual assembly. This constraint hinders the miniaturization of the bistable cube. However, we expect SLS can 3D printing

© 2024 The Author(s). Advanced Intelligent Systems published by Wiley-VCH GmbH

the blocks in one piece, which can reduce manual fabrication error and increase building speed.

4. Experimental Section

Fabrication of the Bistable Cube and Applications: The single piece of bistable cube was printed with FDM 3D printer (Raise3D Pro2, Raise3D Technologies Inc) with a 95 A TPU filament (3D Aura Pte Ltd). The printed layer height was 0.1 mm in the slicing software ideaMaker. The six pieces were glued together with instant adhesive (Keydak 833, Keydak Ltd). Caps and connectors of the manipulator and crawler were 3D printed with SLA (Form3, Formlabs Inc) with clear resin (Formlabs Inc) with layer thickness 0.1 mm. After the parts were printed, a thin layer of silicone membrane (Zhongyu Rubber Products Co., Ltd) with thickness of 0.1 mm was covered to the outside of the bistable cubes to provide a pressure chamber for manipulator and crawler and sealed using silicone glue (K-704 Silicone Adhesive, Guangdong Hengda New Materials Technology Co., Ltd). The further details of parameter are reported in Figure S3. More fabrication process details are presented in Figure S8.

Compression test of the Bistable Cube: The compression test of bistable cube was conducted on a universal testing machine (Mark-10 Corp) with a 25 N force sensor under displacement control. Both ends of the bistable cube were gripped with sensor and batch. The loading speed was 0.1 mm s^{-1} with 16 mm displacement.

FE Simulations: The FE simulations were conducted using Abaqus/Static (Dassault Systèmes Simulia Corp). For compression test, we simplified the single piece of bistable cube for easier mesh and separated it into rigid body (almost no strain) and normal body. The elastic modulus of the 3D printed TPU was set to be 78.4 MPa (Figure S1), and Poisson's ratio was set to 0.48 to ensure small material compressibility. To keep boundary conditions same as experimental test, we set smooth steps for vertical locomotion 8 mm at each end and set free conditions for the other two directions. We tied each piece in their contact area.

Soft Robotic Application Control: We used a STM32-474RE to control a six-channel relay (G2RL-2, Shenzhen Biaokong Electric Technology Co., Ltd), which connected to three 5/3 solenoid valves (VK332V-5 G-01, SMC Corp), as shown in Figure 4a. A vacuum pump (G4BL2490-2 T, Shanghai Pengpu Fluid Technology Co., Ltd) was connected to the valves to provide negative pressure up to −90 kPa. A pressure pump (TC-320) was connected to the valves to provide positive pressure up to 20 kPa. The control system for the tube crawler was same with the manipulator system which means three chambers (Figure 5c) connected to three 5/3 solenoid valves; also, a loop digital input set for crawler locomotion.

We subsequently proposed a human-in-the-loop closed-loop control algorithm (Figure S5) to investigate the locomotion performance of the manipulator. The manipulator is intended to follow the command $u_{\text{cmd}} = [u^x, u^y]$ provided by the human operator to track motions in 3D space. We first project all the possible 3D positions in Euclidean space into the length of the three chambers $S_i = [s_i^1, s_i^2, s_i^3]$, where $i \in [1, 216]$ is the index of all the combinations of the chamber. Herein, s_i^j, with $j \in [1, 2, 3]$ is encoded within the range of $[0, 1]$. These states are then appended with the corresponding command input $u_{\text{in}} = [u^x, u^y]$. The ground truth of $\{S_i, u_{\text{in}}\}$ was meticulously collected and labeled prior to the experiment. In the course of testing, the operator's intent is estimated through $i^* = \arg\min \|u_{\text{in}} - u_{\text{cmd}}\|_2$, leading to the determination of the corresponding state $S_i = [s_i^1, s_i^2, s_i^3]$. The current state $S_c = [s_c^1, s_c^2, s_c^3]$ is inferred by a mapping from the vision-based sensory system $S_c = f(p)$, where p is the captured raw sensor input. Consequently, the relays' controls are determined straightforwardly by $u_{\text{out}} = sign(sat(S_{i^*} - S_c))$. The term *sat* denotes a saturation function, notably simpler than the Proportional-Integral-Derivative (PID) controller, which is a significant benefit from the bistable structure. When $|S_{i^*} - S_c|$ is small, the system seamlessly transitions into a locked state, thereby mitigating the intricacies associated with control precision and diminishing the shock on the manipulator's mechanical response.

Supporting Information

Supporting Information is available from the Wiley Online Library or from the author.

Acknowledgements

This work was supported by the A*STAR Singapore through RIE2025 MTC IRG Award M21K2c0118 and by Singapore MOE Tier-2 Award MOE-T2EP50123-0015. Y.W. acknowledges the NAP award 020482 from Nanyang Technological University Singapore.

Conflict of Interest

The authors declare no conflict of interest.

Author Contributions

Bojian Zhang: Conceptualization (lead); Data curation (lead); Formal analysis (lead); Investigation (lead); Methodology (lead); Software (lead); Validation (lead); Visualization (lead); Writing—original draft (lead); Writing—review and editing (lead). **Zhiqiang Meng**: Investigation (supporting); Methodology (supporting); Software (supporting); Validation (supporting); Writing—original draft (supporting); Writing—review and editing (supporting). **Xudong Yang**: Investigation (supporting); Methodology (supporting); Software (supporting); Validation (supporting); Writing—original draft (supporting). **Yiran Zhang**: Investigation (supporting); Software (supporting). **Tianyu Chen**: Investigation (supporting); Software (supporting); Writing—original draft (supporting). **Yu Chen**: Investigation (supporting); Software (supporting); Writing—original draft (supporting). **Yifan Wang**: Conceptualization (lead); Formal analysis (equal); Funding acquisition (lead); Investigation (lead); Methodology (lead); Project administration (lead); Resources (lead); Supervision (lead); Writing—original draft (equal); Writing—review and editing (equal).

Data Availability Statement

The data that support the findings of this study are available from the corresponding author upon reasonable request.

Keywords

3D bistable structures, auxetic blocks, multistable robotics, programmable bistability

Received: June 26, 2024
Published online: August 4, 2024

[1] A. Pal, V. Restrepo, D. Goswami, R. V. Martinez, *Adv. Mater.* **2021**, *33*, 2006939.
[2] L. Hines, K. Petersen, G. Z. Lum, M. Sitti, *Adv. Mater.* **2017**, *29*, 1603483.
[3] B. Gorissen, D. Reynaerts, S. Konishi, K. Yoshida, J.-W. Kim, M. De Volder, *Adv. Mater.* **2017**, *29*, 1604977.
[4] X. Yang, Z. Wang, B. Zhang, T. Chen, C. Linghu, K. Wu, G. Wang, H. Wang, Y. Wang, *Adv. Intell. Syst.* **2023**, *5*, 2200250.
[5] D. Rus, M. T. Tolley, *Nature* **2015**, *521*, 467.
[6] C. Laschi, B. Mazzolai, M. Cianchetti, *Sci. Robot.* **2016**, *1*, eaah3690.
[7] Y. Wang, L. Li, D. Hofmann, J. E. Andrade, C. Daraio, *Nature* **2021**, *596*, 238.

© 2024 The Author(s). Advanced Intelligent Systems published by Wiley-VCH GmbH

[8] C. Linghu, Z. Du, Y. Sun, W. Chen, K. J. Hsia, *Extreme Mech. Lett.* **2023**, *64*, 102092.
[9] C. Tawk, G. Alici, *Adv. Intell. Syst.* **2021**, *3*, 2000223.
[10] M. S. Xavier, C. D. Tawk, A. Zolfagharian, J. Pinskier, D. Howard, T. Young, J. Lai, S. M. Harrison, Y. K. Yong, M. Bodaghi, A. J. Fleming, *IEEE Access* **2022**, *10*, 59442.
[11] J. Walker, T. Zidek, C. Harbel, S. Yoon, F. S. Strickland, S. Kumar, M. Shin, *Actuators* **2020**, *9*, 3.
[12] M. S. Verma, A. Ainla, D. Yang, D. Harburg, G. M. Whitesides, *Soft Robot.* **2018**, *5*, 133.
[13] L. Qin, X. Liang, H. Huang, C. K. Chui, R. C.-H. Yeow, J. Zhu, *Soft Robot.* **2019**, *6*, 455.
[14] A. Rafsanjani, Y. Zhang, B. Liu, S. M. Rubinstein, K. Bertoldi, *Sci. Robot.* **2018**, *3*, eaar7555.
[15] A. D. Marchese, R. K. Katzschmann, D. Rus, *Soft Robot.* **2015**, *2*, 7.
[16] S. Rahman, L. Wu, A. El Elmi, D. Pasini, *Adv. Funct. Mater.* **2023**, *33*, 2304151.
[17] M. A. Robertson, J. Paik, *Sci. Robot.* **2017**, *2*, eaan6357.
[18] C. Zhang, Z. Zhang, Y. Peng, Y. Zhang, S. An, Y. Wang, Z. Zhai, Y. Xu, H. Jiang, *Nat. Commun.* **2023**, *14*, 4329.
[19] D. Melancon, A. E. Forte, L. M. Kamp, B. Gorissen, K. Bertoldi, *Adv. Funct. Mater.* **2022**, *32*, 2201891.
[20] A. Pal, M. Sitti, *Proc. Natl. Acad. Sci. U.S.A.* **2023**, *120*, e2212489120.
[21] J. R. Raney, N. Nadkarni, C. Daraio, D. M. Kochmann, J. A. Lewis, K. Bertoldi, *Proc. Natl. Acad. Sci. U.S.A.* **2016**, *113*, 9722.
[22] T. Chen, K. Shea, *3D Print. Addit. Manuf.* **2018**, *5*, 91.
[23] Q. He, R. Yin, Y. Hua, W. Jiao, C. Mo, H. Shu, J. R. Raney, *Sci. Adv.* **2023**, *9*, eade9247.
[24] S. Chen, Y. Cao, M. Sarparast, H. Yuan, L. Dong, X. Tan, C. Cao, *Adv. Mater. Technol.* **2020**, *5*, 1900837.
[25] Z. Zhang, X. Li, X. Yu, H. Chai, Y. Li, H. Wu, S. Jiang, *Compos. Struct.* **2019**, *229*, 111422.
[26] C. Geckeler, S. Mintchev, *Adv. Intell. Syst.* **2022**, *4*, 2200087.
[27] D. K. Patel, X. Huang, Y. Luo, M. Mungekar, M. K. Jawed, L. Yao, C. Majidi, *Adv. Mater. Technol.* **2023**, *8*, 2201259.
[28] Y. Chi, Y. Tang, H. Liu, J. Yin, *Adv. Mater. Technol.* **2020**, *5*, 2000370.
[29] L. Jin, Y. Yang, B. O. T. Maldonado, S. D. Lee, N. Figueroa, R. J. Full, S. Yang, *Adv. Intell. Syst.* **2023**, *5*, 2300039.
[30] B. Gorissen, D. Melancon, N. Vasios, M. Torbati, K. Bertoldi, *Sci. Robot.* **2020**, *5*, eabb1967.
[31] F. Pan, Y. Li, Z. Li, J. Yang, B. Liu, Y. Chen, *Adv. Mater.* **2019**, *31*, 1900548.
[32] Y. Chi, Y. Li, Y. Zhao, Y. Hong, Y. Tang, J. Yin, *Adv. Mater.* **2022**, *34*, 2110384.
[33] J. Shi, H. Mofatteh, A. Mirabolghasemi, G. Desharnais, A. Akbarzadeh, *Adv. Mater.* **2021**, *33*, 2102423.
[34] S. Shan, S. H. Kang, J. R. Raney, P. Wang, L. Fang, F. Candido, J. A. Lewis, K. Bertoldi, *Adv. Mater.* **2015**, *27*, 4296.
[35] G. W. Brodland, H. Cohen, *Int. J. Solids Struct.* **1987**, *23*, 1341.
[36] J. A. Faber, J. P. Udani, K. S. Riley, A. R. Studart, A. F. Arrieta, *Adv. Sci.* **2020**, *7*, 2001955.
[37] D. P. Holmes, A. J. Crosby, *Adv. Mater.* **2007**, *19*, 3589.
[38] M. Taffetani, X. Jiang, D. P. Holmes, D. Vella, *Proc. R. Soc. Math. Phys. Eng. Sci.* **2018**, *474*, 20170910.
[39] Z. Meng, H. Yan, M. Liu, W. Qin, G. M. Genin, C. Q. Chen, *Adv. Sci.* **2023**, *10*, 2301581.
[40] Z. Meng, M. Liu, H. Yan, G. M. Genin, C. Q. Chen, *Sci. Adv.* **2022**, *8*, eabn5460.
[41] H. Jiang, X. Liu, X. Chen, Z. Wang, Y. Jin, X. Chen, *2016 IEEE Int. Conf. Robot. Biomim(ROBIO)*, Qingdao, China **2016**, pp. 350–356.
[42] M. Cianchetti, T. Ranzani, G. Gerboni, T. Nanayakkara, K. Althoefer, P. Dasgupta, A. Menciassi, *Soft Robot.* **2014**, *1*, 122.
[43] Q. Guan, J. Sun, Y. Liu, N. M. Wereley, J. Leng, *Soft Robot.* **2020**, *7*, 597.
[44] X. Dong, D. Axinte, D. Palmer, S. Cobos, M. Raffles, A. Rabani, J. Kell, *Robot. Comput.-Integr. Manuf.* **2017**, *44*, 218.
[45] Q. He, Z. Wang, Y. Wang, A. Minori, M. T. Tolley, S. Cai, *Sci. Adv.* **2019**, *5*, eaax5746.
[46] W. Fan, J. Wang, Z. Zhang, G. Chen, H. Wang, *IEEE/ASME Trans. Mechatron.* **2024**, *1*, 11.

© 2024 The Author(s). Advanced Intelligent Systems published by Wiley-VCH GmbH